Daylight Measurement Acquisition of Defunct Resident Space Objects Combining Active and Passive Electro-Optical Systems

Julian Rodriguez-Villamizar[iD] and Thomas Schildknecht

Abstract—The uncontrolled growing number of resident space objects (RSOs) threatens the safe operation of space-related activities. Since the beginning of the Space Age, outer space is getting populated by objects emerging after breakup events; spare components through launching, orbiting, and aging of satellite missions; collisions between functional or defunct RSOs; or by missions that either completed or began their life cycle. One potential measure toward the sustainable use of outer space may start by preventing collisions between existing RSOs. Collisions between existing RSOs will only exacerbate the current situation, which could lead to a cascade effect known as the Kessler syndrome. In the context of such collisions, the enabling of optical daylight tracking has the potential to reduce the uncertainty of the estimated state vector for each RSO, thus aiding the planning and execution of efficient avoidance maneuvers when a collision is foreseeable, as well as benefiting just-in-time collision avoidance strategies in the future. This study starts by analyzing the impact of optical daylight observations, within the domain of defunct RSOs, with respect to the currently restricted nighttime observation windows, the type of observable acquired by the observing station, and the relative geometry between the Sun, the RSO, and the ground station. We highlight the role of key hardware components on each observing system deemed critical for current observing optical ground stations to enable daylight measurement acquisition. Once we have inspected all factors deemed crucial for daylight observations in our system, we present successful daylight observations, from which we derived angular observables, ranges, and apparent brightness. We additionally provide an example where the combination of measurements acquired by the different systems, operating in the optical regime only, contributed to partial disambiguation of the tumbling motion of a selected rocket body. All observations were conducted using a scientific complementary-metal-oxide-semiconductor (CMOS) sensor and a geodetic laser ranging system. Both systems make use of the 1-m Zimmerwald laser and astrometry telescope (ZIMLAT) for measurement acquisition and target RSO tracking at the Swiss Optical Ground Station and Geodynamics Observatory Zimmerwald (SwissOGS), operated by the Astronomical Institute of the University of Bern, Switzerland.

Index Terms—Active tracking, daylight, laser ranging, passive optical, resident space objects (RSOs).

I. INTRODUCTION: STATE OF THE ART

THE fact that the number of dysfunctional man-made objects in space is higher than the number of fully operational missions is not only worrisome, but also stresses that the current use of the outer space is unsustainable. Most recent figures of merit addressing the number and distribution of different resident space objects (RSOs) in outer space may be found in [1]. The conclusion is clear: the number of RSOs is growing rapidly and this growth represents a higher likelihood of two RSOs being in close proximity, which, in a worst-case scenario, could lead to unavoidable collisions if they are left unaccounted for. One of the current mitigation guidelines issued by the Inter-Agency Space Debris Coordination Committee (IADC) highlights the prevention of such on-orbit collisions [2], based on former studies conducted by The Committee on the Peaceful Uses of Outer Space (COPUOS), among others. To prevent collisions, we need updated state vectors for each RSO, alongside realistic representations of the corresponding uncertainty. To comply with this, ground- and space-based sensors, observing with different techniques, provide measurements that serve as the basis for the construction, update, and refinement of catalogs of RSOs.

One widely employed observing technique is radio detection and ranging (RADAR), which is capable of operating not only through cloud-covered skies, but also during daytime. The latter capability represents an existing data gap for optical observing systems. Historically, the first successful experiments to conduct daylight observations using a passive electro-optical system were reported in [3]. The Ground-Based Electro-Optical Deep Space Surveillance (GEODSS) Experimental Test System (ETS) consisted of a 0.78-m aperture f/5 telescope using a silicon vidicon television camera together with a video processing system that was able to discern RSOs with an apparent magnitude of up to 8.3. In one day, the Group 94 of the Massachusetts Institute of Technology was able to reduce the data acquired from 20 passes, from which 13 were finally sent out to the North American Aerospace Defence Command Space Defence Center for its fusion with radar data for orbit improvement. The group encountered several key problems: first, the tracking angular rates, which was solved by the modification of the servo loop parameters, however, gaps were present in passes crossing the north pole since the equatorial mount of the telescope could not keep up with the angular rates of the RSOs passing through that particular

location. Second, to estimate the sensitivity of detection, the group calculated the visual magnitude of a sunlit Low Earth Orbit (LEO) RSO using the knowledge they acquired from observing, reducing, and calibrating observations to geosynchronous RSOs considering the impact of the phase angle, that is, the angle between the Sun, RSO, and ground station. Their conclusion was that the sensitivity limit needed to be dimmer than an apparent magnitude of 8 to be able to observe RSOs at a range of about 1000 km, indicating modifications were needed in the hardware and software of the nighttime system used until then. As part of the sensitivity study, the group directly measured the diffuse background contribution, which appeared to vary from 3.8 to 5.4 apparent magnitudes per square arcsecond at locations of the sky away from the Sun. Finally, by observing calibrated stars during daylight, they were able to confirm the sensitivity computed for their system to be ten apparent magnitudes, after several iterations of modifying specific components of the hardware and the software. For hardware specifications, including details about the implemented spectral filters, and a comparison between the silicon vidicon and ebsicon (the main sensors available at that time), the reader is referred to [3].

The study presented in [3] served as a baseline for the next incremental technological improvements. In particular, the advent of the charged-couple device (CCD) or complementary metal-oxide-semiconductor (CMOS) imaging detectors, and the exploration of new nonsilicon-based semiconductor material in the sensor's substrate, exploiting a higher quantum efficiency at the sensor level in the near- and short-wave infrared spectral regions. Studies conducted exploring these options are provided in [4], [5] and focus on the observation of geosynchronous, geostationary (GEO), and LEO RSOs. Note that while the presented work in [5] focuses more on observation strategies to maximize the signal-to-noise ratio of LEO RSOs, by analyzing the phase and aspect angles, as well as the impact of the atmosphere, the work in [4] reports a complete, commercially available, passive system solution that demonstrates an optimized system transmission in the short-wave infrared region, in addition to an improvement in the detector characteristics with a customized cooling system. Additionally, the authors in [6] report a thorough optimization of a passive electro-optical system for daylight observations of LEO RSOs. Their study comprises the quantification of the sky background contribution for a given passive electro-optical system, combined with an in-depth study of an optimal hardware configuration regarding the detector pixel size and the focal ratio. The main driver of this optimal configuration is given by the observed portion of the sky that must contain a predefined number of stars, with a minimum observable magnitude, to be able to plate solve the acquired images, and hence derive astrometric measurements from them.

Besides the unprecedented technical achievements presented in [3], there are two other factors that are critical and have been further expanded in recent studies: the signal processing system and the astrometric reduction of the acquired images. Successful daylight imaging systems are characterized by a small field of view, relatively large aperture telescopes, short exposure times, and high frame acquisition rates. Short integration times become mandatory to avoid saturating the detector. Techniques such as lucky imaging, that is, the combination of frames acquired at high readout speed and low exposures to increase the angular resolution of the image, will help in the discrimination and detection of the RSO. Further information concerning lucky imaging and variations thereof used in the domain of defunct RSOs are available, for example, in [7]. Finally, the second factor concerns the astrometric reduction of the data, which consists of the determination of the coordinates in the image with respect to a given reference frame, for example, the International Celestial Reference Frame. Currently, there are two possibilities to solve the orientation of the camera reference frame: either to determine it on the fly, if there are enough reference stars at the acquisition time, or to use the pointing information derived from the angular encoders in the telescope. Due to the narrow field of view available in current successful systems, the fact that we are targeting LEO RSOs and that stars dimmer than an eight apparent magnitude will not be easily discernible, the second option seems to be more attractive. The use of such a technique has been reported in [4], [8].

Laser beams of active electro-optical systems have fields of view of tens of arcseconds, requiring extremely accurate ephemerides that are currently not available for most RSOs. To compensate for this, one approach might be to use a passive aiding optical target acquisition system that will correct the pointing of the telescope to lock the RSO within the field of view of the laser beam. Once we ensure that we are collimating the laser beam on the RSO, the next challenge concerns discriminating between the photons backscattered from the RSO, those coming from the background, and those produced by thermal current in the detector. At the system level, analysis of daylight active electro-optical systems can be found, for example, in [9], [10]. Note that the first reference alludes to RSOs carrying a highly reflective element onboard, such as a retroreflector; those RSOs are also known as cooperative RSOs, while the absence of highly reflective elements onboard the RSOs corresponds to the so-called noncooperative RSOs. Successful retrieval of a signal reflected by noncooperative RSOs during daylight was presented in [11].

In this work, we study the impact of daylight observations at the level of information gain for the domain of defunct RSOs, and at the technical level specific to the Swiss Optical Ground Station and Geodynamics Observatory Zimmerwald (SwissOGS), for which the capabilities have been expanded to enable measurement acquisition during daylight with a passive and active electro-optical system. Specifically, we start with an in-depth analysis focused on the current geographic distribution of optical systems and their current available nighttime observation windows for one year. We then analyze the impact of observations for the defunct Environmental Satellite (ENVISAT), for which there is currently a substantial optical data gap for European ground-based observatories during the summer season. The impact of the data gap is addressed from the point of view of a full state vector comprising not only the orbital elements, but also the attitude state and its motion. At the technical level, we study the contribution of the diffuse daylight sky background in our optical systems. For both

active and passive electro-optical systems, we quantify the signal-to-noise ratio, which permits the identification of critical components, both in software and hardware, and allows us to identify RSOs in current existing catalogs for which we expect a high detection probability. Finally, we present raw measurements acquired by our systems, stressing factors not directly accounted for during the analytical study of the signal-to-noise ratio, but rather from the knowledge acquired during an extensive experimental phase. In addition, we present a case study where the simultaneous observation of the RSO with an active and passive electro-optical system allowed us to partially disambiguate its tumbling motion after being tracked at the SwissOGS.

II. Impact of Daylight Observations in the Monitoring of Defunct RSOs

In this section, we present potential benefits in current observing space surveillance and tracking networks, achieved by enabling the acquisition of daylight observations. Within the scope of this study, we define surveillance and tracking as the capability of a sensor to retrieve observables of different natures to create, complete, or refine RSO orbits and attitude catalogs. These catalogs will establish the basis for computing collision probabilities and the monitoring of RSO-specific attitude states. The number and type of observations, provided by the sensors, will play a crucial role in the estimation of the attitude of the targeted RSO, its evolution in time, as well as the estimation of realistic collision probabilities derived from updated state vectors using precise and accurate measurements; the latter being critical to, for example, perform efficient avoidance maneuvers between RSOs. In Sections II-A–II-C, we present three arguments that highlight the relevance of daylight observations in the framework of space surveillance and tracking.

A. Length of Day

In general, the observation of defunct RSOs with altitudes between 400 and 2000 km by a passive electro-optical system is restricted to the twilight zones, that is, dusk and dawn. During these zones, the RSO is expected to be sunlit with a sufficient signal-to-noise ratio, thus enabling the discrimination of the RSO from the sky background. When using an active system such as laser ranging, the sunlit condition is not mandatory, but the rather small field of view of the laser beam demands high accuracy predictions, which are not usually available in the domain of defunct RSOs. Hence, the system needs a passive optical system to correct the pointing of the telescope. Note that we exclude the possibility of blind tracking, that is, the systematic search of an RSO according to a defined pattern, since, in principle, it will be dominated by luck. In the following, we study the relationship between the geographical distribution of current observing sites and the length of the day in the pursuit of an extension of the current observing twilight time windows.

Most of the current dedicated optical ground stations are concentrated in the mid-latitudes of the northern hemisphere. Examples of the distribution of such networks are given by

the International Scientific Optical Network (ISON) [12], for the passive electro-optical case, and by the International Laser Ranging Service (ILRS) [13] for the active electro-optical; note that from the ILRS, only selected stations are able to observe either cooperative RSOs during daylight, or noncooperative RSOs with high-power dedicated defunct RSO lasers. Even though there are recent developments in tracking networks with better geographical distribution, such as the small aperture robotic telescope network (SMARTnet) [14], the productivity of such observing networks is restricted mainly to night observation sessions. The main problem becomes evident: the summer season for mid-latitudes, both in the northern and southern hemispheres, is critical due to the long daylight hours. Enabling the daylight measurement acquisition capability will result in a significant productivity gain. Nevertheless, the relationship between available observing hours and actual useful observations is not straightforward for optical sensors. Critical factors involving the local weather, the configuration of Sun–RSO–station and its evolution with respect to time, or even air traffic (only for active electro-optical) could prevent the observation during certain timeslots within the available observing hours.

B. Attitude Determination

Within the surveillance of outer space, the information about the attitude state of RSOs and its change in time is critical for on-orbit servicing and active defunct RSOs removal initiatives. These initiatives address the direct disposal of defunct RSOs via direct momentum transfer using either space- or ground-based lasers [15], drag augmentation devices in the form of foam or sales [16], or by using catching devices, for example, grapplers [17]. Other types of initiatives propose the on-orbit repairing, refueling, stabilizing, or even helping in the deployment of specific components that became unresponsive, such as antennas or solar panels [17]. Using either active or passive observing systems, we can retrieve evidence of the attitude state at each observation epoch, which is deemed critical prior information to any mentioned on-orbit servicing activities. Examples of attitude determination using passive optical systems can be found in [18]. Likewise, a comprehensive attitude study using only an active electro-optical system was reported in [19].

Successful observations conducted during daylight could provide additional information about the RSO's state, that is, orbital elements and attitude motion. For all state-vector updates, catalog maintenance, and close approach analysis, including maneuver planning and execution, this additional information may come from observables of different natures, that is, ranges and angular measurements to be used in an orbit determination, or improvement, step. For all attitude-related analyses, this additional information may come either from the different illumination conditions or from the observation at different aspect angles.

C. Observation Geometry and Orbital Arc

The impact of the observed orbital arc and the measurement type on orbit determination and improvement of defunct RSOs

has been shown in [20]. Furthermore, studies focused on single-pass solutions varying the number and distribution of the observations within passes over the station at different culminations can be found in [21]. Note that we describe the length of the arc with respect to the revolution period. The results from the aforementioned studies highlight and recommend the observation of longer arcs, that is, as long as possible, and data fusion between observables of different natures, that is, angles and ranges, for an improvement in orbital accuracy of orders of magnitudes.

In this section, we focus on the observable arc from one single station, the SwissOGS, to perform the visibility study of the decommissioned ENVISAT. The following study applies to any other RSO, but the choice of ENVISAT is driven by the RSO being a representative defunct RSO from the congested Sun-synchronous orbital regime [22]. The main characteristics of this orbital type are first that the orientation of the orbital plane with respect to the Sun remains constant in time, and second, by being a polar orbit, it assures coverage of the entire globe. The two aforementioned features are attractive for Earth observation missions that have equal on-ground illumination conditions for each revisiting ground track of the satellite over the same locations. The latest space environment report issued by the European Space Agency [1] shows worrisome numbers corresponding to close conjunctions between RSOs in that specific orbital regime, thus providing a reasonable motivation to study the impact of daylight observations for ENVISAT, from which its uncontrolled disintegration, for an object with a mass of 8110 kg, could generate a cloud of debris posing a threat to all existing, or potential future, missions.

We start by analyzing the ground track of the satellite. The orbital parameters were extracted from the latest Two Line Element set available in [23]. The orbital elements were propagated for 36 h, with their associated Simplified General Perturbations model 4 (SGP4) analytical propagator storing the state vector every 10 s. The resulting state vectors were transformed into the Earth-centered-Earth-fixed reference frame being represented as ground tracks in Fig. 1. Likewise, we represent in magenta the tracks that are visible from the SwissOGS, which correspond to passes with a minimum elevation of 20° over the station. For the 36 h of propagation, there are five passes over the SwissOGS for a satellite with a revolution period of about 100.2 min. Of all passes, four out of five are ascending passes (south–north direction) and one is a descending pass; the latter is the longest observable pass from all. Fig. 1 highlights the importance of a global tracking network since most the revolutions are left untracked using only one station. For the monitoring of ENVISAT, the nonupdated state vectors will change significantly in time due to both a lack of observations between revolutions, as well as gravitational and nongravitational perturbations acting on an RSO flying at an altitude of about 770 km. Note that the nongravitational perturbations, such as solar radiation pressure and air drag, will act on an average cross section of 74 m^2. The poor predictions derived from the nonupdated state vectors will challenge observatories to do follow-up observation strategies with limited field-of-view sensors, such as laser ranging systems.
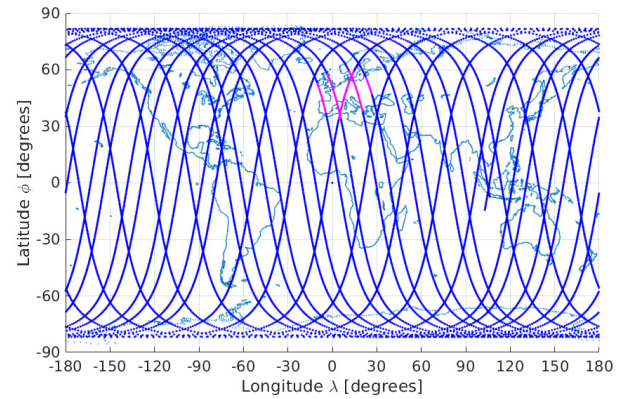

Fig. 1. Ground track of ENVISAT starting on July 28, 2021, at 10:00 Coordinated Universal Time (UTC) until July 29, 2021, at 22:00 UTC. The orbital elements were extracted from the latest two line element (TLE) set available from [23] at starting date. The segments of the track represented in magenta depict the portion of the orbit observed from the SwissOGS using an elevation mask of 20°.

Next, we check the observability conditions of those passes from the SwissOGS, assuming a cloudless sky and dedicated passive and active electro-optical systems.

Fig. 2 shows a sky plot corresponding to the five passes of ENVISAT that are visible from the SwissOGS. The beginning and end of the passes are marked with a cross and a dot, respectively, to indicate the flight direction. The five passes might be further classified into three high culmination passes (light and dark blue, dark red), and two low culmination (purple and yellow). The time of each pass is displayed in the box in Fig. 2, from which we can immediately see that all available passes occur during daylight. Note that the low culmination passes will be significantly affected by extinction effects due to a larger air mass and the attenuation due to larger distances of the RSO with respect to the station. To ensure the observability of any pass, we computed the position of the Sun over the SwissOGS at the starting epoch of each pass. Comparing the entries in Table I with Fig. 2, we see that the observation conditions for the first pass are excellent, reaching a phase angle of about 90° at the culmination of the RSO. The observation of the second pass will be challenging since there is inferior conjunction between the Sun, the RSO, and the observer, that is, a phase angle of nearly 180° shortly after the culmination of the RSO. For the third pass, the alignment between the three bodies is in inferior conjunction, but the culmination of the pass by the RSO is nearly at the zenith, which gives an angular distance from the position of the Sun reducing the amount of sky background. The fourth pass has a similar configuration as described for the first pass. Finally, for the fifth pass, there will be an azimuthal encounter between the telescope and Sun, but a difference in elevation of about 30°. From all passes, it is reasonable to expect that during nearly inferior conjunctions, there will be a gap in observations due to the sky background contribution and large phase angles, which compromise the amount of signal-to-noise ratio on the observation site.

From this analysis, we can conclude that observation geometry plays a critical role in daylight observations. The impact

TABLE I
HORIZONTAL COORDINATES OF THE SUN AT THE STARTING EPOCH OF VISIBLE PASSES FOR ENVISAT OVER THE SWISSOGS

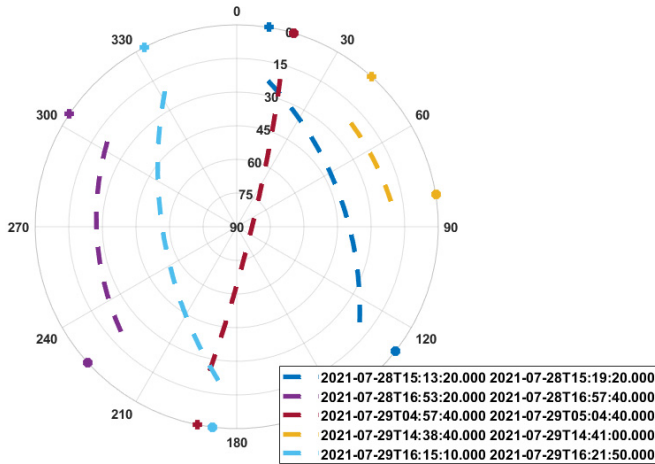| Start pass UTC	Azimuth [deg]	Elevation [deg]
2021-07-28T15:13:20	256.529	37.901
2021-07-28T16:53:20	275.565	20.912
2021-07-29T04:57:40	70.200	7.140
2021-07-29T14:38:40	248.465	43.376
2021-07-29T16:15:10	268.520	27.260

Fig. 2. Sky plot centered at the SwissOGS for ENVISAT starting on July 28, 2021, at 10:00 UTC until July 29, 2021, at 22:00 UTC. The hours of each pass are shown at the bottom-right of the plot in UTC. The beginning and end of the pass are marked with a cross and a dot, respectively, to indicate the flight direction.

Fig. 3. Observed orbital arc in Fig. 2 represented in the orbit reference frame. Colors match with the passes displayed in Fig. 2.

of the atmosphere, the distance between the satellite and the station, and the phase angle, both from the illumination and sky background contribution, will determine the observability of the pass. Nevertheless, the observation during daylight using passive and active optical systems will allow us to monitor arcs of the orbit of ENVISAT, which would otherwise not be accessible.

The last part of this section focuses on the length of the observed arc and its distribution along the orbit of ENVISAT. Fig. 3 represents each potential observable pass at the SwissOGS (Fig. 2) in the orbit reference frame. The highest culmination passes shown in Fig. 2 not only cover the largest portion of the orbit in Fig. 3, but also have a better distribution over the orbit. On the other hand, all except the longest arc fall into nearly the same portion of the orbit. The consequence of using only passes over the same portion of the orbit is that the predictions for stations observing that portion will most likely be better than predictions for stations observing the opposite portion of the orbit.

From the analysis of the observation geometry, the arc length, and the distribution of observations along the orbital arc, it becomes clear that a tailored observation session can be optimized to maximize productivity while still achieving high-quality observations. The latter is crucial for an orbit determination or improvement, which will permit the reacquisition of the RSO by the same or other observing stations. For the case of observations from ENVISAT for one single station, two
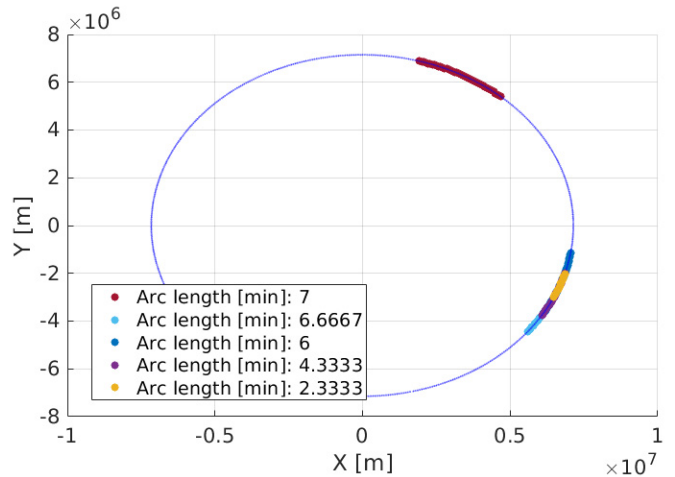
passes corresponding to ascending and descending observable passes cover the largest portion of the orbit with the best distribution of observations. However, the other passes could be useful for attitude state analysis, since the illumination conditions and aspect angles are different.

III. METHODOLOGY

The observation of RSOs, with both active and passive electro-optical systems, during daylight requires the adaptation and enhancement of specific hardware and software components. In this section, we formulate the problem analytically, provide numerical calculations using the technical specification of each system available at the SwissOGS, and compare the results against real observations. The contribution of this section is to show the agreement between the resulting figures of merit derived from the theoretical modeling, with the figures obtained from real observations. The latter is deemed critical since it permits an *a priori* study of the system's behavior after the modification of specific components, parameterized with the theoretical model. All implemented changes are new for both active and passive electro-optical systems at the SwissOGS. Furthermore, from the relationships derived from the analytical models and observations, the scalability of the problem is addressed in terms of minimum detectable RSO size for our optical ground station, representing an optimal filter given the current size of the RSO population.

A. Mitigation of Background Noise in Passive Electro-Optical Systems

We derive the observed number of solar photons per unit time at a given direction for a passive electro-optical system using the following equation:

$$B_p = \int_{400}^{800} Q(\lambda)_{\text{eff}} \; \eta_{\text{rx}} \; \Omega_{\text{rec}} \; \cos(\theta) \; A_{\text{rec}} \; B(\lambda)_{\text{diff}} \; d\lambda \quad (1)$$

where B_p is the diffuse solar radiance measured on the passive optical receiver, $Q(\lambda)_{\text{eff}}$ is the quantum efficiency
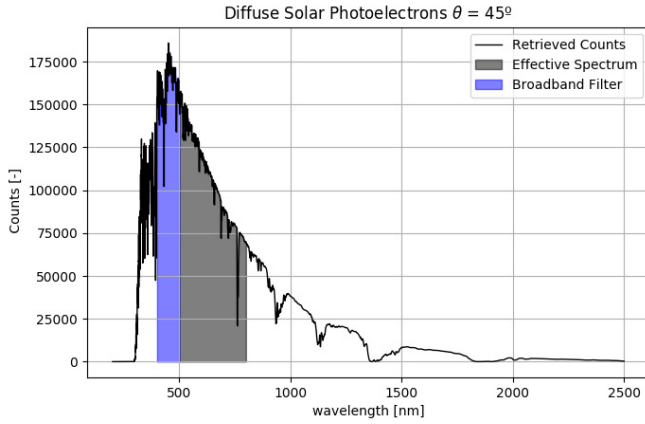
Fig. 4. Count of triggered photoelectrons after incident solar diffuse spectral radiance on the receiver using an integration time of 0.01 s. The plot shows the area removed by using a spectral broadband rectangular filter from 400 to 500 nm and the remaining portion of the visible spectrum. The diffuse solar radiation direction is that of 45° away from the direct incidence.
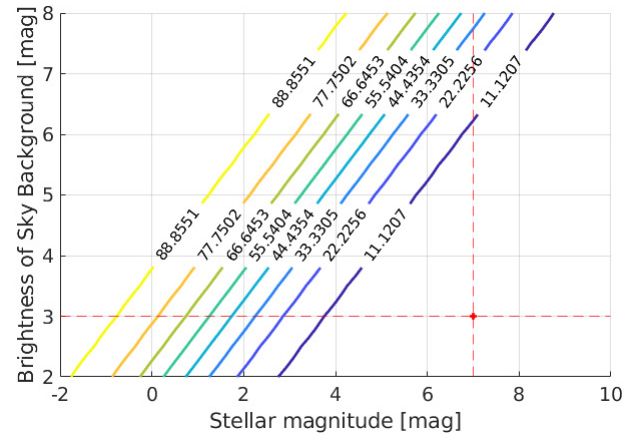

Fig. 5. Percentage of incoming starlight as a function of the daylight sky background with magnitudes ranging from 2 to 8 and stars within a magnitude range from −2 to 10. The dashed red lines indicate the limiting magnitudes for a daylight sky background of 2.9 magnitudes; it shows that up to stars with a magnitude of 7, the percentage of incoming starlight is larger than 1%.

of the sensor as a function of the wavelength, η_{rx} is the efficiency of the imaging system (i.e., the receiving optical chain), and $\Omega_{rec} \cos(\theta)$ is the field of view of the sensor; the factor $\cos(\theta)$ is included since the power received at an angle to the normal is proportional to Ω_{rec} in a unit sphere and therefore to the cosine of that angle θ, as per Lambert's cosine law. A_{rec} is the effective aperture area of the telescope, and $B(\lambda)_{diff}$ is the on-ground spectral solar radiance, which was derived using the low-resolution-atmospheric-transmission (LOWTRAN) software package based on the code in [24], further enhanced with the new modules provided in [25].

In order to estimate the expected photoelectrons triggered by the diffuse solar spectral radiance on the receiver, we solve (1) numerically using Simpson's numerical integration scheme. All system specifications, which are station-dependent, are given in Appendix A.

The retrieved counts per wavelength, corresponding to the integrand in (1), are shown in Fig. 4. We estimated a total theoretical number of counts of 31 547 and 16 043 per imaging pixel, without and with the use of a broadband rectangular filter between 400 and 500 nm, respectively. To validate the previous theoretical estimates, we conducted daylight observations of stars with angular distances of nearly 45° with respect to the Sun, consistent with the values used for the theoretical modeling. From the measurements acquired from two different stars, the estimated background level in terms of counts per pixel was 34 248 and 38 420 without the broadband rectangular filter. We, therefore, conclude that the modeling of the sky radiance is in good agreement with the observed one, showing an average error of 13%.

In a second step, we estimated fluxes via aperture photometry for both stars, and by using the standard value of the magnitude for each reference star, we derived the relative magnitude between the reference star and background, yielding $\Delta_{star_1}^{bck} = -0.8$ for the reference star of two magnitudes and $\Delta_{star_2}^{bck} = 3.5$ for the reference star of 6.5 magnitudes. The average background magnitude was estimated to be 2.9, which is in agreement with the values found in the literature [26].

To find the limiting observable magnitude, which is needed later on to find the minimum observable size of an RSO, we used the previously calculated magnitude of the daylight sky background and computed the percentage of incoming starlight by varying the magnitude of stars, as done in [27]. In our computations, we allow for variations in the background from 2 to 9 magnitudes. Furthermore, using the atmospheric seeing [28] as a first-order approximation of the resulting point spread function of the star in the image plane, we can derive limiting magnitudes for daylight observations as shown in Fig. 5. Note that in Fig. 5, an atmospheric seeing value of 2 arcsec was chosen, since it is the average seeing at the SwissOGS. Worse seeing conditions, which are expected during the daytime, will set the limiting observing magnitude to brighter values.

According to Fig. 5, we are limited to detect RSOs fainter than a magnitude of 7 for daylight observations with a sky background contribution of 2.9 magnitudes, since the amount of incoming starlight is less than 1%, a value found through empirical experimentation for recognizing the RSO on the image by the naked eye. First results after observing stars with varying magnitudes were presented at the ILRS Technical Workshop in October 2019, showing good agreement with the theoretical findings [29].

From this section, we present the following conclusions.

1) The use of a blocking filter from 400 to 500 nm can reduce the impact of the resulting diffuse solar photons on the receiver by 50%. The implementation of this type of broadband filter attenuates the largest sky background contribution (see Fig. 4) compared to the amount of sunlight reflected by the RSO assuming that the RSO does not have favorable optical properties between 400 and 500 nm (see spectral signature examples of different RSO in [30]). In comparison to the results from previous studies (see [6]), we have a specific detector already available, and thus the optimization came from the point of view of minimizing the impact of the sky background in the spectral bands where the contribution was highest.

TABLE II
ON-RECEIVER DIFFUSE SOLAR RADIANCE AT 532 nm

	$B(\lambda_{532})_{diff}$
$\theta = 10°$	219 W/sr m^2 μm
$\theta = 45°$	81 W/sr m^2 μm
$\theta = 60°$	68 W/sr m^2 μm

2) In (1), we see that the on-site sky background radiance is proportional to the field of view. Likewise, the field of view is inversely proportional to the focal length. Therefore, by using a larger focal length, we reduce the field of view of a single pixel, and thus the contribution of the sky background on the detector. At the system level, we changed the focal length from 4 to 8 m.

3) The observation of passes in inferior conjunction must be avoided to prevent the saturation of the detector. Alternatively, the implementation and execution of a maneuver while observing the remaining part of the pass should occur. In our system, that feature was implemented at the telescope control level as the minimum angular distance between the pointing direction and the position of the Sun in the sky—currently set up at 25°.

B. Mitigation of Background Noise in Active Electro-Optical Systems

The estimation of triggered photoelectrons from the diffuse solar photons collected by the receiver particularized for a specific wavelength, in our case 532 nm after frequency doubling of the fundamental 1064 nm, reads

$$B_{A_{532}} = \int_{532-0.05}^{532+0.05} Q(\lambda_{532})_{\text{eff}} \ \eta_{\text{rx}} \ \Omega_{\text{rec}} \ \cos(\theta) \ A_{\text{rec}}$$
$$\times B(\lambda_{532})_{\text{diff}} d\lambda \quad (2)$$

where the only difference with respect to (1) is that we take the diffuse solar radiance and quantum efficiency at that specific wavelength of 532 nm, the operational wavelength of our laser ranging system, and the limits of integration correspond to the spectral width of 1 angstrom from the used narrowband filter. In addition, the emitted laser pulses are shifted in wavelength due to the relative motion of the RSO with respect to the tracking station, natural broadening, Doppler broadening—in this case, due to the thermal motion of the radiating source—and collision broadening, but fall into a second-order change in the emitted wavelength if compared to the width of the employed narrowband filter.

In Table II, we show the diffuse solar flux at 532 nm, varying the angular distance θ between the pointing of the telescope and the location of the Sun in the sky over the station.

Taking $\theta = 10°$ as a worst-case scenario, we calculate, by solving (2), a mean diffuse solar photoelectron flux rate of 21 MHz. The most favorable scenario, $\theta = 60°$, yields photoelectron rates of 3 MHz. Our findings agree with the values provided in [10]. Note that during daylight, the dark counts ($\approx$120 kHz) are negligible compared to the observed rate of photoelectrons triggered from the sky background.

The solar photoelectrons will affect the identification of the backscattered photons from the RSO, particularly for RSOs that do not carry retroreflectors onboard, that is, noncooperative RSOs.

All conclusions given for passive-optical systems apply also to active ones. The only difference, regarding blocking filters, is that for active systems, we use narrowband filters instead of broadband ones. Specific adaptations of our system include:

1) The reduction of the field of view in the receiving optical chain through an iris of variable aperture—adjustable diameter between 10 and 40 arcseconds.

2) The use of the 1064-nm wavelength (see Fig. 4), which is less sensitive to the diffuse solar radiation contribution.

3) The use of a gated receiver may further reduce the impact of solar photons by setting small range gates, that is, temporal windows, at the expected return epoch of the emitted pulse. However, in order to fully exploit that capability, accurate ephemerides are needed, which is not usually the case with defunct RSOs.

C. Minimum Observable RSO

To derive the minimum observable RSO size, we consider in the analysis: the geometrical cross section, orbital regime, optical properties of the targeted RSO—in particular, the albedo and the reflectance—and the detection capabilities by a passive and active electro-optical system.

In the case of passive electro-optical systems, the reflected radiation by an RSO illuminated by the Sun is given by [31]

$$E_{\text{rso}} = \frac{E_0 \pi \ \sigma_{\text{rso}} \phi(\Theta) \rho \alpha}{16 \pi \ R_{\text{sln}}^2} \quad (3)$$

where E_{rso} is the reflected radiation by the RSO, E_0 is the incident direct radiation from the Sun, σ_{rso} is the cross section of the RSO, R_{sln} is the slant range of the RSO with respect to the observing station, $\phi(\Theta)$ is the phase function, with Θ as phase angle, ρ is the albedo of the RSO, and α is the reflectivity. By using the apparent magnitude of a known star, in this case, the Sun, we can derive the relative magnitude of interest using the expression

$$M_{\text{rso}} = M_{\text{sun}} - 2.5 \log\left(\frac{E_{\text{rso}}}{E_0}\right) \quad (4)$$

where M_{sun} is the apparent magnitude of the Sun within the visible spectrum of -26.74 [32] and M_{rso} is the apparent magnitude of the RSO of interest—here, we input the value computed previously as limiting magnitude. By combining and rearranging (3) and (4), we can derive the RSO cross section, yielding the following expression:

$$\sqrt{\sigma_{\text{rso}}} = R_{\text{sln}} 10^{\frac{M_{\text{rso}} - M_{\text{sun}} - 2.5*\log(16 \cdot 10^{-10} \ \phi(\theta) \rho \ \alpha)}{-4.5}} \quad (5)$$

where σ_{rso} is the radius corresponding to the geometrical cross section of the RSO, R_{sln} is the slant range, and M_{rso} the apparent brightness of the RSO. Taking an average albedo of 0.2 [33], a near zenith pointing and an elevation of 30° for the elevation of the Sun, which yields $\phi(70) = 0.11$ rad, the minimum observable defunct RSO, with an apparent

magnitude of 7 at 400 km, has a radius of 14 cm. At 2000 km, the minimum observable RSO has a radius of 69 cm.

For the estimation of the minimum observable RSO size using an active system, we make use of the so-called radar link equation [34]

$$E_{rx} = \frac{E_{tx} G_{tx} \sigma_{rso} A_{rec} \eta_{tx} \eta_{rx} \eta_{qe} T_{atm}^2}{\left(4\pi R_{sl}^2\right)^2} \tag{6}$$

where E_{rx} is the expected power measured at the receiver, E_{tx} is the emitted power, G_{tx} is the transmission gain, σ_{rso} is the cross section of the RSO, A_{rec} is the receiver aperture effective area, R_{sl} is the slant range station-RSO, η_{tx} is the efficiency of the transmission in the optical chain, η_{rx} is the efficiency of the receiving optical chain, η_{qe} is the quantum efficiency of the detector, and T_{atm} is the one-way atmospheric transmission. Bear in mind that 6 assumes that the distance between RSO and an observing station, besides the atmospheric conditions, did not change significantly within the round trip of the signal, either for antennas, or telescopes, working in a monostatic configuration, that is, the same telescope for transmitting and receiving the signal. For bistatic or multistatic configurations, those assumptions must be revised. Next, we consider a new taxonomy, according to σ_{rso}, including those RSOs that carry highly reflective elements onboard, for example, retroreflectors, which in some cases were optimized optically at the most common wavelength used by the network of tracking stations of the ILRS (532 nm). We distinguish between:

1) *Cooperative:* RSOs that carry retroreflectors onboard and have a controllable or stable attitude. This group is comprised mainly of active missions. The order of magnitude of the optical cross section is 10^6 m^2 estimated within ILRS activities [13].

2) *Pseudo-cooperative:* RSOs that carry a retroreflector, or a highly reflective element onboard, but have an unstable or unknown attitude. These RSOs are mainly decommissioned satellites. Presumably, the optical cross section is in the order of 10^6 m^2, but aging effects, unstable attitude, and unknown geometry between the line of sight and reflective elements may vary the expected optical cross section.

3) *Noncooperative:* RSOs that do not carry a retroreflector onboard and have presumably unknown optical properties and attitude. The order of magnitude for the optical cross section is 10^0 m^2. Note that the radar cross section is often used to approximate the optical cross section despite the different interactions between the scattering properties of the RSO and each radiation regime.

The next question is: how can one determine a photon budget for any RSO if there is presumably no knowledge of its cross section? Our approach consists of selecting a cooperative RSO with a known optical cross section, from which we obtained reliable return rates from past observations. Together with the technical specifications of the station, we can calculate its expected return rate by solving 6. Likewise, we set up the equation for the RSO. Having the two equations, we divide the budget equation for the cooperative RSO by the budget equation for the noncooperative one. We can then solve for

the optical cross section of the RSO. The quotient of the two-photon budget equations yields

$$\frac{E_{rx}|_{lag}}{E_{rx}|_{rso}} = \frac{R_{rx}|_{lag}^4}{R_{rx}|_{rso}^4} \frac{\sigma_{lag}}{\sigma_{rso}} \zeta \tag{7}$$

where $E_{rx}|_{lag}$ is the expected return rate in photoelectrons per second for the reference RSO, for example, the Laser Geodynamics Satellite 1 (LAGEOS-1) and $E_{rx}|_{rso}$ for the RSO, $R_{rx}|_{lag}$ and $R_{rx}|_{rso}$ correspond to the slant range of both LAGEOS-1 and the RSO, σ_{lag} and σ_{rso} are the cross sections for LAGEOS-1 and the RSO, respectively, and ζ is the ratio between the gain as a function of configuration parameters, such as beam divergence, pointing accuracy, tracking jitter, and so on, which may change per RSO. To solve for σ_{rso} in 7, the parameters that have to be fixed are $E_{rx}|_{rso}$ and $R_{rx}|_{rso}$. Note that the value plugged in for $E_{rx}|_{rso}$ is defined mainly by the threshold used to discriminate the signal from the noise, which can be formulated using only the knowledge from the noise (see 2). Fixing $E_{rx}|_{rso}$ to two photoelectrons per second, and setting $E_{rx}|_{lag} = 7$ photoelectrons per second from the estimated return rates for LAGEOS-1, we calculate the estimated cross sections of RSOs with varying altitudes at different elevation angles.

For the correct interpretation of the results, several considerations must be made. First, in (7), if $\zeta = 1$ the system configuration, that is, beam divergence and output power, is exactly the same for both references (LAGEOS-1) and relative RSO. Nevertheless, the pointing of the telescope to LAGEOS-1 is favored due to the availability of accurate ephemerides, as well as the geometrical shape and dimensions of the RSO. For ranging to defunct RSOs, we enhanced the pointing of the telescope using a passive electro-optical system, which permits us to collimate the laser beam on the RSO using active tracking. Second, the reference RSO was chosen to be LAGEOS-1 since return rates higher than 10% are further attenuated, via a variable neutral density filter on the receiving optical chain, which is the usual scenario when observing LEO RSOs with our system. The resulting effect may hide the elevation dependency, which has a clear impact on the observed return rate. Third, the trend in the observed minus computed measurements coming from the use of inaccurate predictions is neglected. The latter will affect the finding of the actual trace of photoelectrons coming from the RSO with respect to the ones triggered by the background diffuse solar photons.

The main conclusions after deriving cross sections with this method show:

1) High culmination passes will maximize the return rates for the observing station. This information may be used to select passes within a specific observation session that maximize the probability of detection of the RSO backscattered signal.

2) Our system is limited to targets with a minimum cross section larger than 10 m^2 for RSOs flying 500 km above the observing station. This highlights the role of laser systems with a higher power than the one currently available in our system (1 W), for being able to range reliably to pseudo- and noncooperative RSOs.

D. Signal Strengthening

In passive electro-optical observing systems, the signal may be enhanced through the observation of larger RSOs or better illumination conditions; changes in the receiving system will also contribute to enhancements in the sky background contribution. When using active systems, we can analyze the laser output power to increase the backscattered signal reflected by the RSO. After inspecting 6, given an emitted power E_{tx}, the received power E_{rx}, coming from a monochromatic, highly directed radiation beam, is proportional to the inverse of the solid angle subtended by the intersecting RSO with the beam. Considering the two-way radiation path, and assuming the same distance station-RSO, one derives the free-space loss, which is proportional to the inverse of the fourth power of the distance station-RSO. The impact of the free-space loss for an orbiting satellite at an altitude of 1000 km is in the order of 10^{-24}. Furthermore, assuming ideal transmit–receiving optical chains, atmospheric transmission, a telescope with an effective area of 1 m^2, and an optical cross section of 1 m^2, the received power is 8. 10 $^{-14}$ W, after the emission of 1 W. Subjected to the previous premises, we can strengthen the budget by including the transmitting gain G_{tx}, which may be computed rigorously to account for off-axis intensity distribution and obscured telescope apertures. Assuming that the laser source is operating in the lowest cavity mode, that is, TEM00, and that the antenna gain patterns are measured in the far-field, the transmitting gain can be expressed as [35]

$$G_{tx} = \frac{2}{\pi R_{sl}^2 \theta_{div}^2} e^{-2\frac{\theta_{div}^2}{\theta_{poi}^2}} \quad (8)$$

where θ_{div} is the beam divergence, θ_{poi} is the pointing error, and R_{sl} is the slant range. To understand the impact of the pointing error and beam divergence, we compare the ratio between 8 and a unit power spherical radiator

$$\frac{1}{4\pi R_{sl}^2}. \quad (9)$$

The results are shown in Fig. 6 as the pointing accuracy and beam divergence are varied.

The conclusion is clear: the use of minimum beam divergence when the pointing of the telescope is inaccurate severely affects the transmitting gain and therefore the received power. Following the previous conclusion, potential recommendations to mitigate the laser pointing error are:

1) In the near field, verify the alignment between the peak of the laser beam profile and the optical axis of the passive acquisition telescope.
2) In the far-field, model the alignment of the optical axis of the passive acquisition telescope, with respect to the maximum laser system response, by observing geodetic cannon-like satellites at distances larger than 3000 km, from which the observing station has a history of return rates corresponding to passes with varying relative geometry between the RSO and the station.
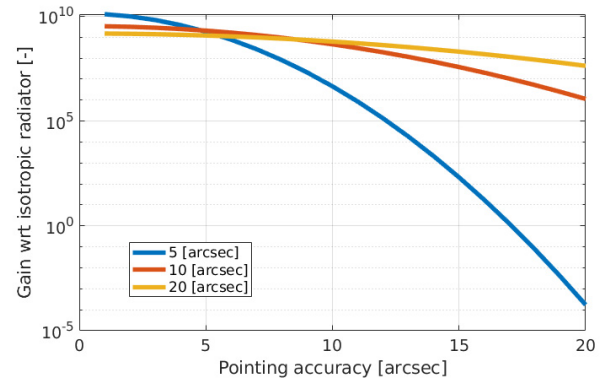3) If the RSO is sunlit, the use of a tracking camera might help to collimate the laser beam on the RSO.

Fig. 6. Antenna gain as a function of the beam divergence and pointing accuracy with respect to a unit power isotropic radiator.

IV. RESULTS

So far, we have developed the conceptual hardware basis to optimize the observation of RSOs during daylight for both passive and active electro-optical systems. In this section, we present examples of daylight observations of RSOs acquired at the SwissOGS. Moreover, we will present one case study where we were able to acquire simultaneously angular measurements, ranges, and brightness from a rocket body. All presented cases are novel and represent the major contribution of this work.

A. Target Selection

One outcome of the previous section corresponds to the selection of RSOs, from which we may expect a signal-to-noise ratio that will permit the identification of the object. However, in Section II, the different dependencies regarding relative geometry and illumination conditions were demonstrated to be an important factor for passive systems. For active systems, the employment of sources with an output power in the order of 1 W will compromise the link budget, especially when ranging to the so-called noncooperative RSOs. From all passes observed at the SwissOGS from our internal catalog, we provide specific examples of objects that are currently regarded as highly relevant within the context of space situational awareness and space traffic management. We present observations from the following targets:

1) *ENVISAT With Cospar Identification Number 2002-009A:* Its orbital regime and body dynamics are of interest due to its size and mass, but the development of potential contingency plans requires an updated state, that is, up-to-date orbital and attitude-related information. The retrieval of regular updates of its state is a missing gap during the summer season for mid-latitude northern nighttime optical observatories: there might be gaps of months, impeding the determination of an updated state. In the following sections, we will provide unprecedented daylight light curves acquired for this object, which were used to estimate the synodic period of the RSO.
2) *TanDEM-X and TerraSAR-X With Cospar Identification Numbers 2010-030A and 2007-026A, Respectively:* This

duo is of particular interest for two reasons. First, both satellites have Sun-synchronous orbits, flying at an equatorial altitude of about 512 km. Second, although TanDEM-X and TerraSAR-X are not decommissioned satellites, they show the potential capability for tracking close approaches between RSOs that could occur as a result of relative formation flying for active defunct RSOs removal or in-orbit servicing initiatives.

3) *Zenit-2 Second Upper Stage With Cospar Identification Number 2007-029B:* This rocket body flies at an altitude of 850 km and provides one example, among the total available in our data pool, with a relatively high signal-to-noise ratio.

4) *Topex/Poseidon 1992-052A:* This defunct satellite is of interest due to its attitude motion, from which we derive evidence utilizing active or passive systems. Note that the target is pseudo-cooperative, thus permitting its observation with traditional geodetic laser systems (output power in the order of 1 W). The availability of measurements acquired from two independent techniques permits the validation and extension of attitude and attitude motion models.

5) *L-55 (YF24) (Long March (CZ) 2C) With Cospar Identification Numbers 2004-046B and 2007-010B, Respectively:* These rocket bodies are interesting since evidence suggests the presence of on-board highly reflective elements. The same motivation as for Topex/Poseidon applies for these RSOs, but the different geometrical shapes, optical properties, and orbital regimes provide new test cases for consolidating attitude and attitude motion models derived from only optical data.

B. Passive Observations

First, we show two passes of the decommissioned satellite ENVISAT that were successfully observed during daylight at the SwissOGS. The average frame rate of the passive electro-optical observations for both passes was of 5 frames/second. The exposure time used for both passes was 0.01 s. Fig. 7 shows the raw light curve of ENVISAT acquired on April 15, 2021, at 5:02 UTC. From the upper plot in Fig. 7, we can see periodicities that might correlate with the synodic period of the RSO; on the bottom plot, we can see that the pass had a high culmination; in addition, the Sun was rising with an elevation of only 2.4°. Fig. 8 shows the raw light curve of ENVISAT acquired on April 24, 2021, at 15:46 UTC. It is interesting to see how at the end of the light curve in Fig. 8, the instrumental magnitudes depict more scattering, which may be explained by a lower signal-to-noise ratio due to an increase in the sky background brightness. By comparing Figs. 7 and 8, we can see presumably different attitude states, or aspect angles, in each pass, further verified after detrending the raw measurements from the phase angle, the station-RSO geometry, and the air mass effect, the latter being a function of the elevation. Furthermore, the illumination conditions are different since the observation geometry with respect to the illuminating source was different each day. The synodic spin period was estimated using the detrended magnitudes with the Lomb-Scargle [36] and the
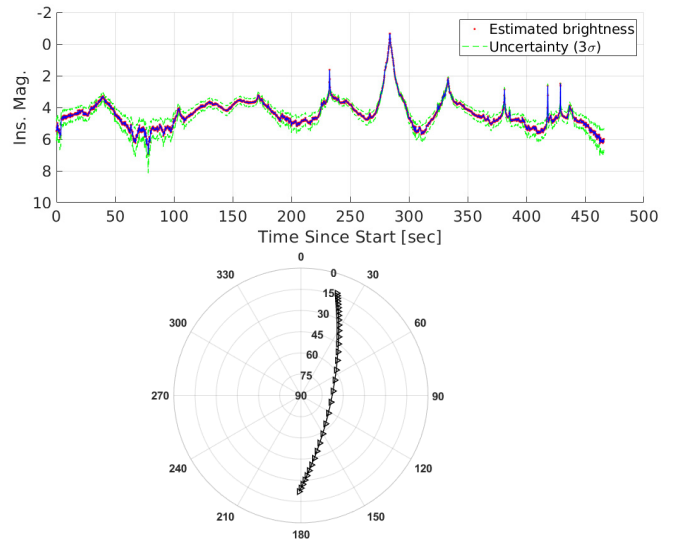

Fig. 7. Light curve of ENVISAT observed on April 15, 2021, during daylight. The elevation of the Sun was 2.4° at the beginning of the observation time, that is, at 5:02 UTC. The top plot shows the changes in brightness of the RSO while crossing the SwissOGS. The geometry of the pass with respect to the observing station is shown in the bottom plot as azimuth and elevation in the horizon system centered at the SwissOGS.
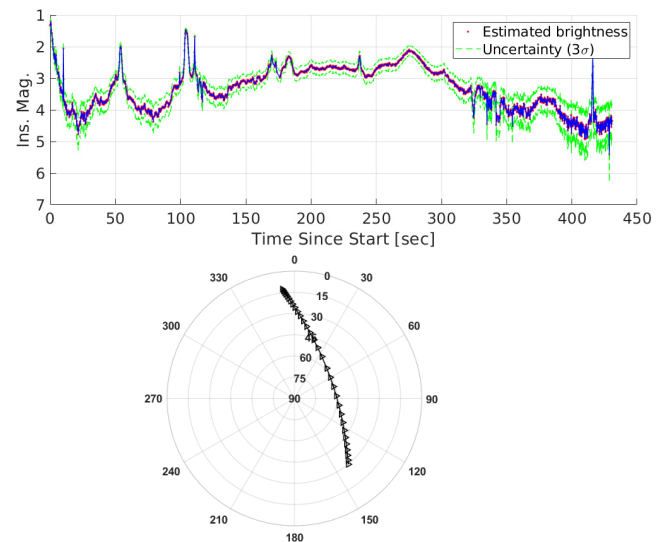

Fig. 8. Light curve of ENVISAT observed on April 24, 2021, during daylight. The elevation of the Sun was 26.9° at the beginning of the observation time, that is, at 15:46 UTC. The top plot shows the changes in brightness of the RSO while crossing the SwissOGS. The geometry of the pass with respect to the observing station is shown in the bottom plot as azimuth and elevation in the horizon system centered at the SwissOGS.

phase dispersion minimization (PDM) [37] methods, using two different procedures as cross-validation of our estimations. The spin periods estimated by both methods are shown in Table III.

Despite the results shown in Table III, we recommend that further observations are performed, since the estimated synodic spin period corresponds to nearly half the total duration of the observed complete pass. To further disambiguate the tumbling motion of ENVISAT, neighboring stations to the SwissOGS could track the RSO before, or after, observable

Pass	Lomb-Scargle	PDM
2021/04/15	230.5 ± 1 [s]	230.1 ± 0.1 [s]
2021/04/24	202.6 ± 1 [s]	226.7 ± 0.5 [s]

passes, which will extend the total duration of each pass, that is, coverage of a longer arc, allowing a more reliable estimation of the synodic spin period.

Second, in Fig. 9, we show two raw frames acquired for three RSOs: TanDEM-X and TerraSAR-X (top plot in Fig. 9) and the Zenit-2 second upper stage (Zenit-2M) (bottom plot in Fig. 9). Note that the measurements for the top plot were acquired on August 28, 2019, at 16:52 UTC and for the bottom plot were acquired on October 16, 2019, at 10:49 UTC. For both days, the apparent position of the Sun was that of 244°, 33° in azimuth, and 139°, 25° in elevation. The exposure time for the top plot in Fig. 9 was set to 0.02 s, while for the bottom plot this was set to 0.04 s. The extracted averaged number of counts per pixel for TanDEM-X (upper RSO in the top plot in Fig. 9) and TerraSAR-X (bottom RSO in the top plot in Fig. 9) were 488 and 421, respectively. On the other hand, the background in terms of counts per pixel for both RSOs was found to be 22 470 and 22 988, which clearly shows the dominance of the brightness of the daylight sky background. Nevertheless, for the used exposure time for this frame, only 38% of the dynamic range was used, suggesting that we could further enhance the signal-to-noise ratio.

To provide a better insight from the previous calculations, we show in Fig. 10 an example of the estimated apertures for both source and background, with the normalized intensity profile as a function of the estimated centroid (further details could be found in [8]). From the representation of the point-like source on the image plane, we see in Fig. 10 speckles caused primarily due to the short exposure time and the fast changes in the refractive index of the atmosphere. Considering the intensity profile, we can see how scattered the observed pixels are with respect to the retrieved point spread function. The explanation is given by the low signal-to-noise ratio.

The extracted number of averaged counts per pixel for Zenit-2M is 1514. Likewise, the counts per pixel from the sky background were estimated to be 23 280, which still shows a dominant sky background per pixel, but with higher signal content for the source if compared to the previous case. The dynamic range in this case is of 47% of the total available, suggesting that we could have increased the exposure time to better exploit the different gray levels given by the 16-bit radiometric resolution of the sensor.

We highlight that for the case of multiple RSOs within the main frame, as shown in Fig. 9, we are able to retrieve the angular measurements for both RSOs. Despite the available individual measurements, the relative angular position of one RSO with respect to the other may be introduced as an observable for computing the relative trajectory of the RSO with respect to, for example, the chaser—after a
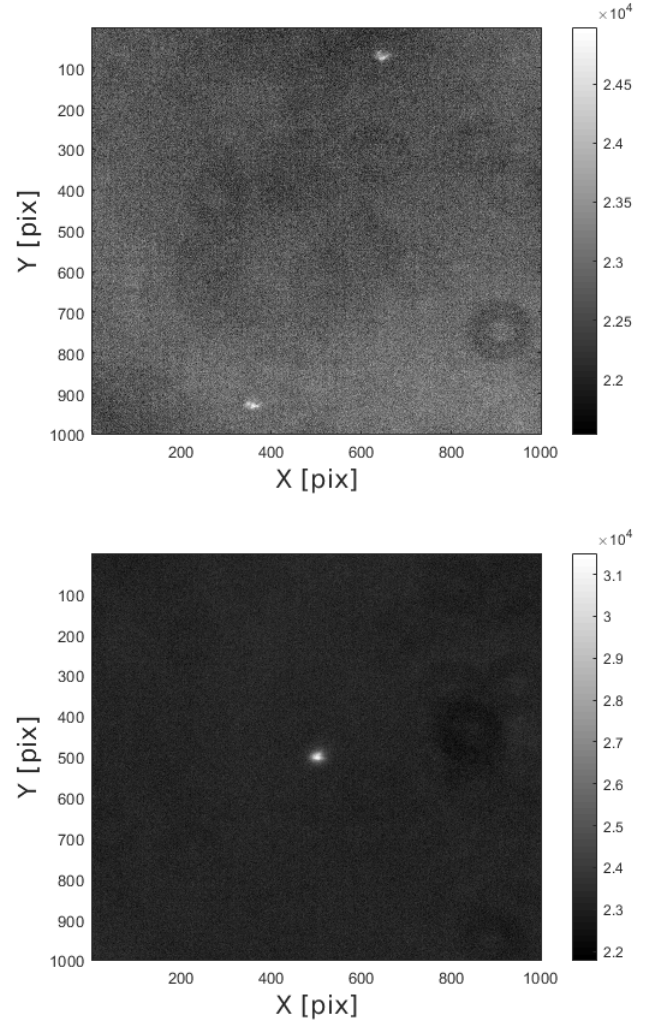

Fig. 9. Examples of subframes acquired during daylight for TanDEM-X and TerraSAR-X (top plot) and the second-stage Zenit-2 (bottom plot). The RSOs were observed on August 28, 2019, at 16:52 UTC (top) and on October 16, 2019, at 10:49 UTC (bottom). For both days, the apparent position of the Sun was that of 244°, 33°, and 139°, 25° in azimuth and elevation, respectively. Units of colorbars: analog–digital units (ADUs PDM).

suitable transformation into the chaser satellite-fixed reference frame.

C. Active Observations

The geodetic satellite laser ranging system at the SwissOGS has been expanded for the tracking of defunct RSOs. In Sections III-B and III-D, we presented novelties regarding the system modifications at the hardware level. Additionally, in [38], we reported further changes at the software level.

In Fig. 11, we show two examples that correspond to the observations of Topex/Poseidon (top plot in Fig. 11) and L-55 (YF24) (Long March (CZ) 2C) (bottom plot in Fig. 11). From the taxonomy defined in Section III-C, both RSOs belong to the pseudo-cooperative category; moreover, the two pseudo-cooperative RSOs are one decommissioned mission, Topex/Poseidon, and one rocket body, Long March. All passes had a high culmination and were observed on August 18, 2021, at 16:18 UTC and August 15, 2020, at 18:47 UTC. On both
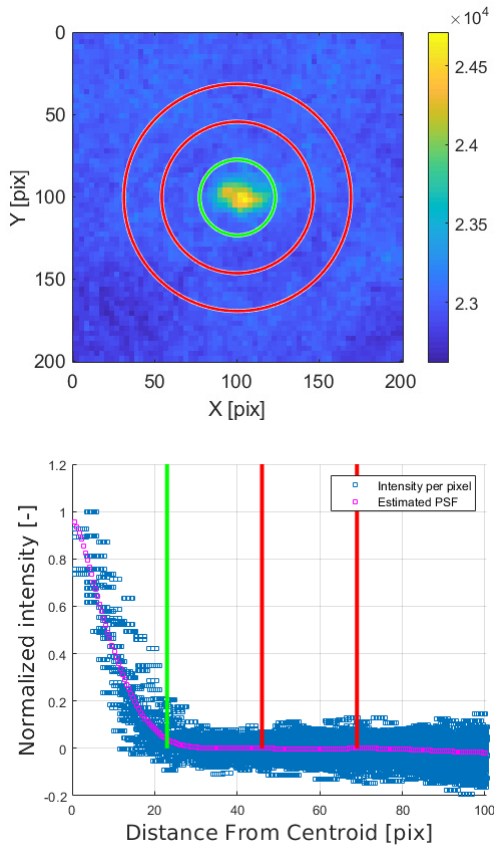
Fig. 10.   Top plot: RSO image and estimated apertures on the image plane; the green circle represents the aperture for the source TerraSAR-X, while the red annulus represents the area sampled to estimate the background. The unit of the color bar is given in ADU. Bottom plot: normalized intensity profile as a function of the estimated centroid with the resulting estimated point spread function.
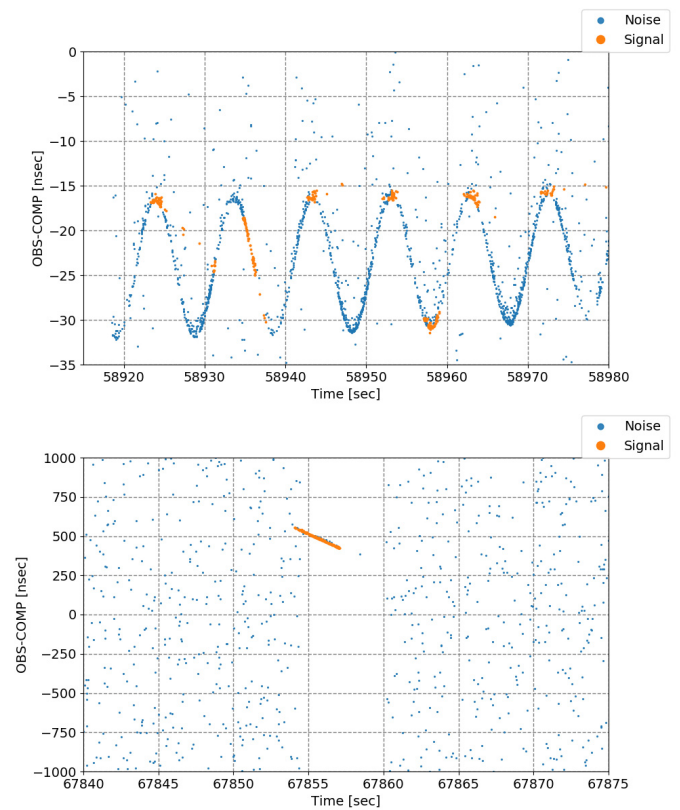

Fig. 11.   Top: detail of triggered photoelectrons on receiver showing the entries classified by noise (blue) and the entries classified as signal (orange) by the real-time filter to the decommissioned satellite Topex/Poseidon on August 18 at 16:18 UTC. The sinusoidal pattern reflects the rotation of the retroreflector with respect to the center of mass of the RSO. This plot exemplifies how the tumbling motion of an RSO can pose a difficulty for the real-time laser ranging filter detector. Bottom: detail of classified photoelectrons in spite of a trace showing a significant slope, about Δ observed measurement (OBS)-computed observation (COM) = 200 ns per 5 s, due to the quality of the used ephemerides for the rocket body L-55 (YF24) (Long March (CZ) 2C) observed on August 15, 2020, at 18:47 UTC.

dates, the azimuth and elevation of the Sun were 238°, 41° and 270°, 18°, respectively.

Before analyzing Fig. 11, we define our digital real-time filter and the criteria used to classify returns into the signal. To find the backscattered signal from the RSO, we check for the distance between at least $N_p/2 + 1$ entries, where N_p is the total number of entries within a predefined sliding temporal window. The distance between entries is defined in two different spaces: the light travel observed-minus-computed time, and the time bias space. The time bias space is defined by the solution of the variational equation of the perigee passing time orbital element for each entry, that is, the quantity that gives the rate of change of the state vector for the RSO due to a change in that particular orbital element (the mathematical derivation is available in [39]). The distances are then compared against RSO-specific prior root-mean-square values, to classify the entries as a signal if the distances of at least $N_p/2+1$ entries are smaller than the *a priori* value. Note that once the procedure finds a signal, the range gate, that is, the temporal window when the returning pulse is expected to trigger an event in the receiver, is reduced and only the perigee passing time coming from the *a priori* orbit is corrected using a Kalman filter as soon as new detections are available.

The top plot in Fig. 11 shows a portion of the observed pass. The clear trace depicted by the real returns reveals the

tumbling motion of Topex/Poseidon. Nevertheless, we see how the tumbling motion affects the detections by the real-time filter. For this particular case, due to the large optical cross section of the RSO, the signal can be easily extracted in a post-processing step. On the other hand, when the photon budget is rather low, we may lose the RSO of interest, which could be totally embedded in photoelectron noise. Note that the laser-ranging observations are providing evidence of the attitude and attitude motion of the retroreflector with respect to the center of mass. The by-product might be used to cross-validate results obtained by different observation techniques using passive electro-optical systems, for example, light curves from only passive data.

Another crucial factor that we identified is given by the quality of the available ephemerides. In the bottom plot in Fig. 11, the signal was found for a very short time, mainly due to the steepness of the trace produced by the RSO's returns. In Section III-C, we derived theoretical minimum observable cross sections, though the attitude station and motion, in addition to the quality of the ephemerides, were not included in the analysis. The last two contributors proved to be relevant for finding the photoelectron trace of the RSO's
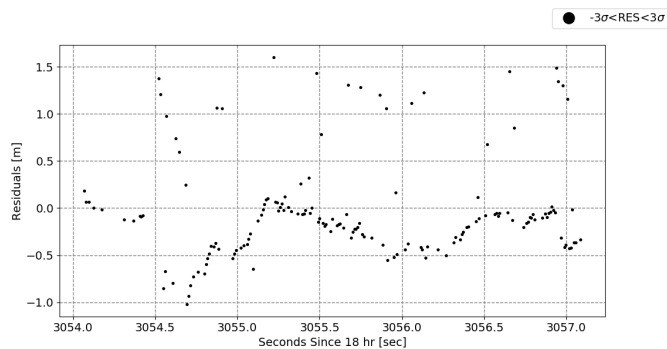
Fig. 12.   Residuals after a constraint-less orbit improvement using one observing station and an ultrashort arc. The bottom trace might correspond to the backscattered signal by a highly reflective element onboard the rocket body, which is a hypothesis supported by the relatively high return rate, while the upper trace might correspond to reflections from either the remaining irradiated portion of the body or a contribution provided by the diffuse reflection of another highly reflective element onboard the rocket body.

backscattered photons in the sea of background photoelectrons. The signal events could only be detected and confirmed after extensive analysis of the data. Despite the short trace detected by our system, shown as a signal in the bottom plot in Fig. 11, we were able to process the acquired measurements and perform an orbit improvement. In Fig. 12, we present the residuals after a constraint-less orbit improvement for the Long March rocket body.

The bottom trace might correspond to the backscattered signal of a highly reflective element onboard the rocket body, for example, a retroreflector, which is a hypothesis supported by the relatively high observed return rate. The upper trace might correspond to reflections either from the remaining part of the irradiated body or by the diffuse reflections of another highly reflective element onboard the rocket body. At second 3054.5, we see a trace of a few measurements that do not correspond to the trend depicted by the two other traces; most likely, these measurements correspond to outliers. The lack of information about the reflective elements onboard the rocket body poses an ambiguity for the interpretation of the results. However, the fact that there are reflecting elements makes this RSO an ideal candidate to perform more regular observations to infer its attitude and attitude motion. Assuming that the upper trace in Fig. 12 comes from the remaining irradiated part of the rocket body, this case highlights the importance of having good ephemerides for the tracking of defunct RSOs with geodetic laser systems. Bear in mind that current geodetic laser systems are about an order of magnitude less powerful than dedicated defunct RSOs laser systems.

D. Simultaneous Combined Observations

Throughout the current study, we have presented selected case studies showing capabilities to observe during daylight using either an active or passive electro-optical system. The outcome of each observation technique is not limited to measurements for orbit improvement, but provides a substantial contribution to the understanding of the attitude and attitude motion of the RSO of interest. Recent developments at the SwissOGS allow the retrieval of measurements acquired by

both passive and active systems simultaneously. One important technical challenge that we overcame, since we are using the same telescope for transmitting and receiving in both active and passive roles, was the temporal alignment between the starting signals for the emission of laser pulses and for exposing the scientific CMOS sensor, which is deemed critical to minimize the impact of laser straylight on the passive system. The time synchronization of the two triggering starting events between the two systems is done via the field-programmable-gate-array device, which adds a short delay for the starting triggering signal on the passive device. Additional challenges were addressed when implementing the Stare and Chase observation strategy reported in [8].

The next case study shows an example of an RSO observed simultaneously by both systems during daylight. The RSO is the rocket body with Cospar identification number 2007-010B. The date of observation was June 12, 2020, at 19:30 UTC, when the Sun was close to the setting. In Fig. 13, we present in the top plot: coordinates in the camera reference frame (X_{cam} and Y_{cam}), which are transformed into horizontal angles by the known transformation [8]; mid-plot: the brightness as a by-product of the active tracking; bottom plot: the observed ranges minus the computed from the predictions acquired with the active system. We start the analysis by focusing on the results from the active tracking and the estimated changes in brightness. From the top plot in Fig. 13, we see the geometrical effects of the tracking in the camera reference frame; the scattering of the measurements is explained by the estimated centroid (see [8] for more details). Moreover, after inspecting the extracted light curve (middle plot in Fig. 13), we can see that there is low scattering in the estimated brightness with respect to time, which translates into a good signal-to-noise ratio. The latter is deemed crucial for a successful RSO recognition of the acquired images in combination with the active tracking phase (see the top plot in Fig. 13) and to retrieve reliable changes in brightness.

The light curve depicts the influence of the geometrical factors, that is, observation geometry between the RSO and the SwissOGS, the geometrical configuration Sun–RSO–station, and the impact of the air mass as a function of the elevation in the horizontal frame. A postprocessing step may provide more insights into the tumbling state of the RSO, since the raw measurements are dominated by the observation conditions. Regarding the observed ranges, we represented the difference between the observed light travel time to the predicted one and binned it into 30-ns periods in the Y-axis, and 1-s periods in the X-axis. Note that the previous operation was done to derive a figure of merit for the concentration of photoelectrons in time and the observed-minus-computed domain, but is not considered a postprocessing step per se. On the right side in the bottom plot in Fig. 13, we can see the highly concentrated photoelectrons depicting a concentration up to five times larger than for the bins that contain presumably noise only. Such a concentration of photoelectrons might be expected for cooperative or pseudo-cooperative RSOs. Despite the high concentration of photoelectrons, there are variations in the consecutive bins along the trace, most likely suggesting an influence on the attitude motion of the RSO. Finally, it is
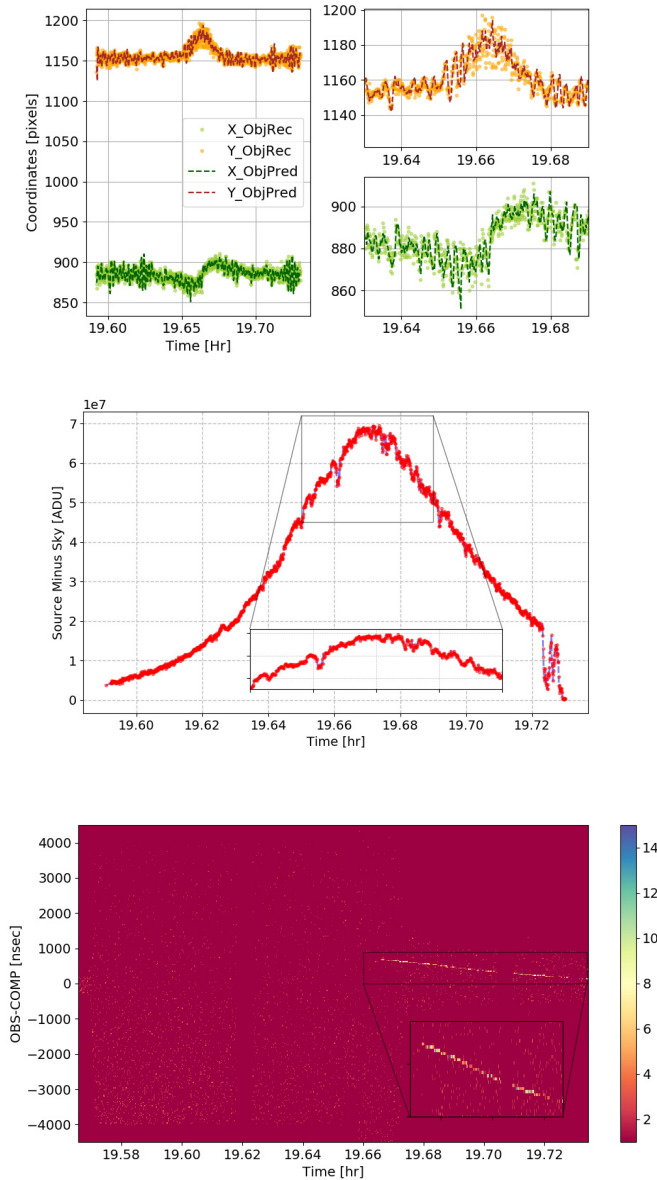
Fig. 13. Top: resulting tracking measurements in the camera reference system for both X and Y after the RSO recognition on the acquired frames by the passive system ObjRec and the prediction ObjPred step estimated by the active tracking module. Mid: resulting light curve for the RSO of interest extracted in real-time while tracking the RSO. The lack of scattering suggests a good signal-to-noise ratio between the source and background. Bottom: resulting active observations after a binning of 30 ns in the Y-axis and 1 s in the X-axis to derive a figure for the concentration of photoelectrons in both domains.

important to notice that for this case, our real-time signal detection algorithm failed. One potential explanation for the failure was found to be the wrong binning size in the Y-axis, which corresponds to the estimated RSO depth.

V. DISCUSSION

The central axis of the presented work was the study of daylight observations from the point of view of information gain in a space situational awareness context, and with more technical regard to the SwissOGS as an optical ground-based observatory. We proved that existing observing and tracking observatories could provide either measurement to update the

state vector of RSOs more regularly, or improved evidence of the attitude and attitude motion via light curves benefiting from different illumination conditions and different attitude states of the targeted RSO along the orbit. There is, nevertheless, one important question to be addressed: will the simultaneous observation of an RSO by a passive and active system add indispensable information compared to the nonsimultaneous observation of the RSO by either system? To answer the formulated question, we present a second pass of the RSO with Cospar identification number 2004-046B observed on July 8, 2020, at 19:33 UTC, where the simultaneous measurement acquisition proved to partially disambiguate the interpretation of the attitude motion of the RSO.

In Fig. 14, we present the real-time light curve (top plot) and one-way range residuals (bottom plot) after orbit improvement. The constraint-less orbit improvement was conducted using the measurements recognized as hits by the real-time laser ranging filter for this pass only. In Fig. 12, we saw that the RSO was providing interesting features possibly related to attitude motion. With the observation of this new pass, we can further explore and propose hypotheses for the attitude and attitude motion, besides insights regarding the optical properties of the RSO.

By inspection of the acquired measurements from both systems, we distinguish at least two positions of the RSO with respect to the observing station. For the first part, starting at 19.59 until 19.64 h, the distribution of the range residuals hardly demonstrates a clear periodic pattern. From the perspective of the passive data, the light curve is dominated mainly by the observation geometry and air mass. For the second part, starting at 19.64 until 19.69, the RSO reveals a local maximum on the passive light curve. In addition, there is evidence of more than one reflective element on the rocket body. The relative maxima on the passive light curve may indicate either the observation of the largest cross section of the rocket body, a favorable phase angle for some reflective parts of the body or a combination of both.

It is interesting to note that changes in brightness do not happen instantaneously, as may occur with RSOs that reflect intense glints or flashes; instead, we can see a progressive increase of the brightness until reaching the maximum, with the corresponding decreasing behavior in a symmetrical fashion. By the end of the pass, the observation conditions turn unfavorable, probably hiding details that we could use for further analysis. From the point of view of the active measurements, we can distinguish at least two traces that might correspond to two highly reflective elements separated with an average distance of about 1 m, and a weak upper trace correlating in trend with the ones of the highly reflective elements, which might correspond to reflected photons by the remaining irradiated part of the body. Finally, the two main traces of the second part show a rotating pattern with a variable amplitude that might correspond to the rotation of the rocket body with respect to the principal axis of the moment of inertia. The experience acquired with the data collected for this particular RSO supports the claim that simultaneous observations, with optical passive and active observing systems, are a valuable asset for the correct understanding
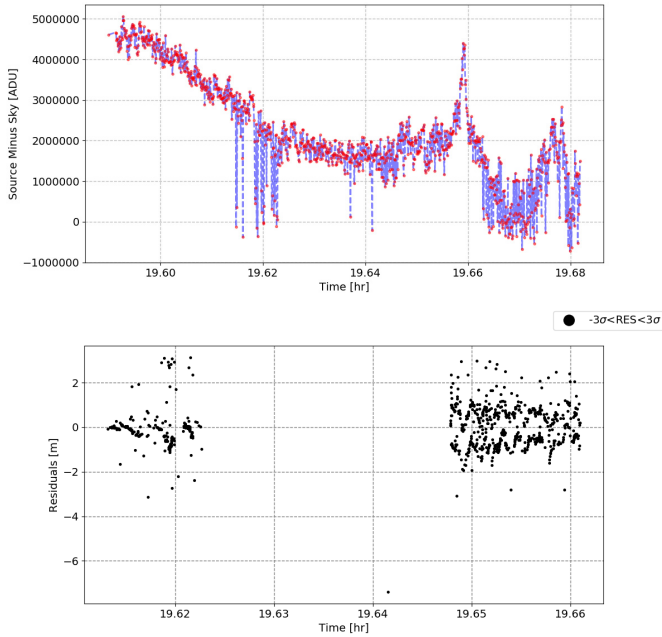
Fig. 14. Top: real-time extracted light curve as a by-product of the active tracking; note that the signature shows a significant scatter coming from a suboptimal signal-to-noise ratio, however, the presence of relative critical points may add information to the understanding of the attitude and attitude motion of the RSO. Bottom: one-way laser ranges residuals after a constraint-less orbit improvement using all detected hits by our laser ranging real-time filter.

and disambiguation of the attitude and attitude motion of RSOs. We are positive that after gathering measurements from several passes, possibly with multiple optical ground-based observing stations, an attitude model for the RSO with Cospar identification number 2004-046B could be proposed, showing an example for the future modeling of attitude states derived from the fusion of only optical data. Here, a key point is an international collaboration between institutions and the joint observation of the RSO.

VI. SUMMARY AND OUTLOOK

The rapidly growing number of RSOs is critical for the safe operation of current and future space missions, which together with the unbalanced ratio between functional and defunct RSO, depict a scenario with a high likelihood of collisions. The prevention of such collisions starts by building up RSO catalogs, which is not possible without the continuous acquisition of measurements by ground and space systems employing different observation techniques. The present work aims to reduce an existing data gap in optical observations due to the technique being restricted to nighttime observations. We presented:

1) *The Impact of Daylight Observations Within the Context of Space Surveillance and Tracking:* Current observation windows for optical sensors are constrained to the observation of RSOs during nighttime only. Those observation windows are further reduced for mid-latitude northern ground stations between equinoxes. We presented examples of light curves from ENVISAT acquired during daylight from which we could exploit different illumination and viewing conditions. The defunct RSO was

chosen conveniently to point out that, due to its orbital configuration, there are currently optical data gaps of months for stations that are not able to observe during daylight. We presented evidence that the contribution of daylight observations aid in reducing this observational gap. Furthermore, the observation during daylight can be optimized to adjust to challenging configurations between Sun–RSO–observer while maximizing the arc coverage and distribution of observed arcs along the orbit.

2) *The Impact of Background Noise and Its Mitigation in Active and Passive Electro-Optical Systems:* The diffuse solar component on the ground was used to derive the number of triggered photoelectrons on the receiver particularized for the systems available at the SwissOGS. Its impact on both active and passive electro-optical systems was analyzed and modifications at the hardware level were presented with the final aim of enhancing existing ground-based optical stations to enable daylight observation capabilities. Furthermore, for the case of passive electro-optical systems, an apparent magnitude of 7 was found to be the limiting magnitude when the brightness of the sky was quantified with an apparent magnitude of 2.9. The theoretical estimates were corroborated with real observations of reference stars. Finally, the use of the near- and short-wave infrared spectral regions, for active and passive optical sensors, would be the preferred choice due to the lower sky background contribution. The efficiency of the transmitting system was analyzed in the near-infrared, reinforcing the idea of further exploiting this specific spectral region for the optical sensors available at the SwissOGS.

3) *The Estimation of the Minimum Observable RSO With Active and Passive Electro-Optical Systems:* In the case of passive systems, we derived a formula (5), from which we can estimate the radius of a geometrical cross section as a function of the apparent magnitude of the RSO, the slant range and assuming a certain phase angle and optical properties of the RSO, such as the albedo and the reflectivity function. In the case of an active system, we used the link budget equation with the technical specifications of our active system, together with a large set of observations to LAGEOS-1, to derive the minimum observable cross section of defunct RSOs, varying the altitude of the RSO and fixing a minimum number of photoelectrons per second at the receiver.

4) *Active and Passive Observations From the Enhanced Systems at the SwissOGS:* Passive observations were acquired of the RSOs TanDEM-X and TerraSAR-X, both within the same frame, stressing the fact that the monitoring of relative formation flying will gain interest rapidly due to on-orbit servicing and active debris removal initiatives. Additionally, observations of the second-stage Zenit-2 were acquired and analyzed using a specific case with a high signal-to-noise ratio. From the active observations, we focused on providing examples that indicate current challenges: in particular, the rather low signal-to-noise ratio when observing

noncooperative RSOs using low power active systems, the tumbling motion, and the quality of the ephemerides of the RSO. Finally, an example proving the capabilities of the simultaneous daylight acquisition was presented.

5) *Usefulness of Simultaneous Combined Active and Passive Electro-Optical Observations:* We presented a case study where the combination of only optical simultaneous observations allowed us to partially disambiguate the tumbling motion of the RSO during the observed pass. The results show that potentially simultaneous observations by several sensors of a network will further contribute to the better understanding and modeling of the attitude dynamics of one of the Long March rocket bodies.

Within future foreseeable activities, we plan a campaign using the passive system for the daylight observation of different stars evenly distributed along the sky. During this campaign, we will attempt to track selected RSOs. We aim to derive conclusions regarding the limiting magnitude of the system, accounting for more variability in the observation conditions. Indirectly, after the reduction of the data, we will estimate geometrical cross sections using the acquired daylight observations. Incoming further developments in our active system comprise the usage of the fundamental frequency of the laser system, that is, 1064 nm, which will not only reduce the diffuse solar background at the receiver level, but will increase the energy of the emitted pulse by a factor of 2 compared to the power in our current system.

APPENDIX

A. Employed Systems and Instrumentation

The Zimmerwald laser and astrometry telescope (ZIMLAT) is a 1-m class Ritchey-Chrétien telescope, with an alt-azimuth mount, used to acquire both active and passive observations. The telescope's effective aperture area is 0.78 m^2; besides the primary and secondary mirrors on the main fork, we use a tertiary and a dichroic mirror permitting the simultaneous acquisition of active (from the laser system) and passive observations of sensors located on the Nasmyth platform. In addition, the nonabsorbed straylight from the laser is filtered by a notch filter centered at 532 $\pm$ 5.3 nm. The impact of the sky background is attenuated through a broadband rectangular filter from 400 to 500 nm. After measuring the system transmittance on the receiving passive optical path, the wavelength-dependent efficiency of ZIMLAT increases from 10% at 400 nm to 60% at 500 nm, yielding a steady value of 80% from 600 until 800 nm. We used the spectral band [400, 800] nm for all theoretical calculations in this work. The pointing of the telescope is modeled by estimating the so-called mount model after observations to reference stars, by specific Satellite Laser Ranging (SLR) RSOs, or by using a tracking camera as shown in [8].

Our passive sensor, installed in one of the focal stations available with a focal length of 8 m, is a scientific CMOS sensor with a given quantum efficiency wavelength-dependent function [40]. The setup yields a field-of-view of 7 arcmin $\times$ 6 arcmin for a chip size of $2.38 \cdot 10^{-4}$ m^2.

Within the active electro-optical system, we can distinguish a laser with a nominal power of 1 W operating at the 532-nm wavelength after frequency doubling of the fundamental wavelength, that is, 1064 nm, with a repetition rate of 100 Hz. The receiving sensor is a compensated single avalanche photodiode (C-SPAD) with a quantum efficiency of 20% at 532 nm. The field of view on the optical chain is regulated through an iris of adjustable aperture currently set up at 10 arcseconds. The receiving optical path is equipped with an air-spaced etalon with a spectral width of 1 nm centered at 532 nm. The efficiency of the receiving optical path was measured using the available measurements from the mirrors on the telescope, multiplied by the efficiency measured in the coudé path using the internal calibration target yielding a value of 50%.

The software used in this work makes use of the SGP4 propagator and internal scripts for the representation of state vectors in different reference frames. The SPG4 model is available, for example, through the [23] website. Information regarding the software and algorithms for the processing of passive optical data is available in [8]. All software related to the postprocessing of laser ranging data, including orbit determination or improvement, is based on a modified version of the software provided and further explained in [41]. In-house tools are provided on reasonable request.

REFERENCES

[1] ESA Space Debris Office. (2020). *ESA's Annual Space Environment Report Revision 4.0.* [Online]. Available: https://www.sdo.esoc.esa.int/environment_report/Space_Environment_Report_latest.pdf

[2] (2020). *Space Debris Mitigation Guidelines, IADC-02-01.* Inter-Agency Space Debris Coordination Committee, Revision 2. [Online]. Available: https://orbitaldebris.jsc.nasa.gov/library/iadc-space-debris-guidelines%-revision-2.pdf

[3] E. W. Rork, S. S. Lin, and A. J. Yakutis, *Ground-Based Electro-Optical Detection of Artificial Satellites in Daylight From Reflected Sunlight.* Cambridge, MA, USA: Massachusetts Institute Technology, 1982.

[4] J. Shaddix *et al.*, "Daytime geo tracking with 'aquila': Approach and results from a new ground-based swir small telescope system," in *Proc. Adv. Maui Opt. Space Surveill. Technol. Conf. (AMOS)*, 2019, pp. 1–12.

[5] N. Estell, D. Ma, and P. Seitzer, "Daylight imaging of LEO satellites using Cots hardware," in *Proc. Adv. Maui Opt. Space Surveill. Technol. Conf. (AMOS)*, 2019, pp. 1–11.

[6] P. Zimmer, J. T. McGraw, and M. R. Ackermann, "Optimizing daylight performance of small visible-NIR optical systems," in *Proc. Adv. Maui Opt. Space Surveill. Technol. Conf.*, 2020, pp. 1–10.

[7] D. Becker and S. Cain, "Improved space object detection using short-exposure image data with daylight background," *Appl. Opt.*, vol. 57, no. 14, pp. 3968–3975, 2018.

[8] J. Rodriguez-Villamizar, E. Cordelli, and T. Schildknecht, "The stare and chase observation strategy at the Swiss Optical Ground Station and Geodynamics Observatory Zimmerwald: From concept to implementation," *Acta Astronautica*, vol. 189, pp. 352–367, Dec. 2021.

[9] F. Yang *et al.*, "Design and observations of satellite laser ranging system for daylight tracking at Shanghai observatory," *Sci. China Ser. A, Math.*, vol. 42, no. 2, pp. 198–206, Feb. 1999.

[10] J. J. Degnan, "Impact of receiver deadtime on photon-counting SLR and altimetry during daylight operations," in *Proc. Int. Workshop Laser Ranging (IWLR)*, 2008, pp. 1–25.

[11] M. A. Steindorfer, G. Kirchner, F. Koidl, P. Wang, B. Jilete, and T. Flohrer, "Daylight space debris laser ranging," *Nature Commun.*, vol. 11, no. 1, p. 6002, Dec. 2019.

[12] I. E. Molotov *et al.*, "Search and study of the space debris and asteroids within ISON project," *Anais Academia Brasileira de Ciências*, vol. 93, no. 1, 2021.

[13] M. R. Pearlman, J. J. Degnan, and J. M. Bosworth, "The international laser ranging service," *Adv. Space Res.*, vol. 30, no. 2, pp. 135–143, Jul. 2002.

[14] H. Fiedler, J. Herzog, M. Prohaska, T. Schildknecht, and M. Weigel, "SMARTnet—Status and statistics," in *Proc. Int. Astron. Congr. (IAC)*, 2017, pp. 1–4.

[15] C. R. Phipps, "A laser-optical system to re-enter or lower low Earth orbit space debris," *Acta Astronautica*, vol. 93, pp. 418–429, Jan. 2014.

[16] M. Andrenucci, P. Pergola, A. Ruggiero, J. Olympio, and L. Summerer, "Active removal of space debris expanding foam application for active debris removal," ESA, Paris, France, Final Rep., 2011.

[17] N. R. Council, *Limiting Future Collision Risk to Spacecraft: An Assessment of NASA's Meteoroid and Orbital Debris Programs*. Washington, DC, USA: National Academies Press, 2011. [Online]. Available: https://nap.nationalacademies.org/catalog/13244/limiting-future-collision-risk-to-spacecraft-an-assessment-of-nasas

[18] J. Šilha, J.-N. Pittet, M. Hamara, and T. Schildknecht, "Apparent rotation properties of space debris extracted from photometric measurements," *Adv. Space Res.*, vol. 61, no. 3, pp. 844–861, Feb. 2018.

[19] J.-N. Pittet, J. Šilha, and T. Schildknecht, "Spin motion determination of the ENVISAT satellite through laser ranging measurements from a single pass measured by a single station," *Adv. Space Res.*, vol. 61, no. 4, pp. 1121–1131, Feb. 2018.

[20] E. Cordelli, A. Vananti, and T. Schildknecht, "Analysis of laser ranges and angular measurements data fusion for space debris orbit determination," *Adv. Space Res.*, vol. 65, no. 1, pp. 419–434, Jan. 2020. [Online]. Available: https://www.sciencedirect.com/science/article/pii/S0273117719308002

[21] J. Rodriguez-Villamizar, E. Cordelli, and T. Schildknecht, "The new stare & chase procedure at the Swiss Optical Ground Station and Geodynamics Observatory Zimmerwald," in *Proc. 1st NEO Debris Detection Conf.*, 2019.

[22] C. Levit and W. Marshall, "Improved orbit predictions using two-line elements," *Adv. Space Res.*, vol. 47, no. 7, pp. 1107–1115, Apr. 2011.

[23] *Space-Track*. Accessed: Oct. 5, 2020. [Online]. Available: https://www.space-track.org/auth/login

[24] F. Kneizys, E. Shettle, W. Gallery, and L. Abreu, "Atmospheric transmittance/radiance: Computer code lowtran 6. Supplement: Program listings," *Environ. Res. Papers*, no. 846, 1983.

[25] F. X. Kneizys, E. Shettle, L. W. Abreu, J. H. Chetwynd, and G. P. Anderson, "User guide to LOWTRAN 7," *Environ. Res. Papers*, no. 1010, 1988.

[26] R. N. Clark, *Visual Astronomy of the Deep Sky*. Cambridge, U.K.: CUP Archive, 1990.

[27] M. Steindorfer, G. Kirchner, F. Koidl, and P. Wang, "Recent space debris related activities at the SLR station Graz," in *Proc. 1st NEO Debris Detection Conf.*, 2019.

[28] F. R. Chromey, *To Measure the Sky: An Introduction to Observational Astronomy*. Cambridge, U.K.: Cambridge Univ. Press, 2010.

[29] E. Cordelli, J. Rodriguez-Villamizar, P. Schlatter, P. Lauber, and T. Schildknecht, *Use of a Night-Tracking Camera During Daytime*. Stuttgart, Germany: ILRS Technical Workshop, 2019.

[30] A. Vananti, T. Schildknecht, and H. Krag, "Reflectance spectroscopy characterization of space debris," *Adv. Space Res.*, vol. 59, no. 10, pp. 2488–2500, May 2017.

[31] T. Flohrer, *Optical Survey Strategies and Their Application to Space Surveillance*. vol. 83, Schweizerischen, Europe: Geodätischen Kommission, 2012.

[32] D. R. Williams, *Sun Fact Sheet*. Accessed: Aug. 1, 2021. [Online]. Available: https://nssdc.gsfc.nasa.gov/planetary/factsheet/sunfact.html

[33] M. Mulrooney, M. Matney, and E. Barker, "A new bond albedo for performing orbital debris brightness to size transformations," in *Proc. Astron. Congr.*, Glasgow, U.K., 2008.

[34] J. J. Degnan, "Millimeter accuracy satellite laser ranging: A review," *Contrib. Space Geodesy Geodynamics, Technol.*, vol. 25, pp. 133–162, Jan. 1993.

[35] B. J. Klein and J. J. Degnan, "Optical antenna gain 1: Transmitting antennas," *Appl. Opt.*, vol. 13, no. 9, p. 2134, 1974.

[36] J. T. VanderPlas, "Understanding the Lomb–Scargle periodogram," *Astrophysical J. Suppl. Ser.*, vol. 236, no. 1, p. 16, May 2018.

[37] R. F. Stellingwerf, "Period determination using phase dispersion minimization," *Astrophysical J.*, vol. 224, p. 953, Sep. 1978.

[38] J. Rodriguez-Villamizar and T. Schildknecht, "Daylight laser ranging of space debris with a geodetic laser from the Swiss Optical Ground Station and Geodyamics Observatory Zimmerwald: First experiences," in *Proc. 8th Eur. Conf. Space Debris (Virtual)*, 2021, pp. 1–8.

[39] G. Beutler, "Methods of celestial mechanics volume I: Physical, mathematical, and numerical principles," in *Astronomy and Astrophysics Library*, 1st ed. Berlin, Germany: Springer, 2010.

[40] Andor Oxford Instruments. *Andor Neo 5.5 sCMOS Specifications*. Accessed: Jan. 17, 2021. [Online]. Available: https://andor.oxinst.com/assets/uploads/products/andor/documents/andor-neo-scmos-specifications.pdf

[41] G. Beutler, L. Mervart, and A. Verdun, "Application to planetary system, geodynamics and satellite geodesy, volume II of methods of celestial mechanics," in *Astronomy and Astrophysics Library*. Cham, Switzerland: Springer, 2005.

Julian Rodriguez-Villamizar received the master's degree in earth oriented space science and technology from the Technical University of Munich, Munich, Germany, and the Ph.D. degree in physics with special qualification in astronomy from the University of Bern, Bern, Switzerland.

Since 2018, he joined the Observation Group at the Swiss Optical Ground Station and Geodynamics Observatory Zimmerwald conducting observations using active and passive systems. He has been involved in space situational awareness related topics after finishing with his master's degree program. His interests include mathematical modeling of physical systems together with the development and implementation of algorithms at low and high levels.

Thomas Schildknecht is currently a leading expert on space debris, space safety, and space sustainability. Under his leadership for more than 25 years, his research group has acquired a World-class expertise in the observation and the characterization of space debris. He is also the Director of the Swiss Optical Ground Station and Geodynamics Observatory Zimmerwald and the Vice-Director of the Astronomical Institute of the University of Berne (AIUB), Bern, Switzerland. At both national and global level, he has served and continues to serve in numerous technical and policy-making committees. Among them for many years as a member of the ESA delegation in the Inter-Agency Space Debris Coordination Committee IADC, where he participated in the negotiations of the IADC Space Debris Mitigation Guidelines. He is a member of the Swiss delegation at UNCOPUOS and substantially contributed to the work of its working group on long-term sustainability of outer space activities. He is currently the Chair of the ESA Space Safety Advisory Group advising the ESA Director responsible for the space safety programme. He is also a full member of the International Academy of Astronautics IAA and the President of the Swiss National Committee of the IAU, and served in the board of several international associations.